Classification and Mutation Prediction from Non-Small Cell Lung Cancer Histopathology Images using Deep Learning

Nicolas Coudray[1,2], Andre L. Moreira[3,4], Theodore Sakellaropoulos[5], David Fenyö[6,7], Narges Razavian[8,*], Aristotelis Tsirigos[1,3,*]

[1] Applied Bioinformatics Laboratories, New York University School of Medicine, NY 10016, USA

[2] Skirball Institue, Dept. of Cell Biology, New York University School of Medicine, NY 10016, USA

[3] Department of Pathology, New York University School of Medicine, NY 10016, USA

[4] Center for Biospecimen Research and Development, New York University, NY 10016, USA

[5] School of Mechanical Engineering, National Technical University of Athens, Zografou 15780, Greece

[6] Institute for Systems Genetics, New York University School of Medicine, NY 10016, USA

[7] Department of Biochemistry and molecular Pharmacology, New York University School of Medicine, NY 10016, USA

[8] Department of Population Health and the Center for Healthcare Innovation and Delivery Science, New York University School of Medicine, NY 10016, USA

* To whom correspondence should be addressed. Tel: +1 646 501 2693; Email: Aristotelis.Tsirigos@nyumc.org; Correspondence may also be addressed to Narges Razavian. Tel: +1 212 263 2234, E-mail: Narges.Razavian@nyumc.org

Abstract

Visual analysis of histopathology slides of lung cell tissues is one of the main methods used by pathologists to assess the stage, types and sub-types of lung cancers. Adenocarcinoma and squamous cell carcinoma are two most prevalent sub-types of lung cancer, but their distinction can be challenging and time-consuming even for the expert eye. In this study, we trained a deep learning convolutional neural network (CNN) model (inception v3) on histopathology images obtained from The Cancer Genome Atlas (TCGA) to accurately classify whole-slide pathology images into adenocarcinoma, squamous cell carcinoma or normal lung tissue. Our method slightly outperforms a human pathologist, achieving better sensitivity and specificity, with ~0.97 average Area Under the Curve (AUC) on a held-out population of whole-slide scans. Furthermore, we trained the neural network to predict the ten most commonly mutated genes in lung adenocarcinoma. We found that six of these genes – STK11, EGFR, FAT1, SETBP1, KRAS and TP53 – can be predicted from pathology images with an accuracy ranging from 0.733 to 0.856, as measured by the AUC on the held-out population. These findings suggest that deep learning models can offer both specialists and patients a fast, accurate and inexpensive detection of cancer types or gene mutations, and thus have a significant impact on cancer treatment.

Keywords

Computational Biology; Cancer; Precision Medicine; Image Analysis; Computer Vision and Pattern Recognitionr; Quantitative Methods; Deep-learning

Introduction

48   According to the American Cancer Society[1], over 150,000 lung cancer patients succumb to their

49   disease each year, while another 200,000 new cases are diagnosed on a yearly basis. It is one

50   of the most widely spread cancers in the world, due mostly to smoking, but also exposure to toxic

51   chemicals like radon, asbestos and arsenic. Non-small cell lung cancers represent 85% of the

52   cases and three sub-types are distinguished: Adenocarcinoma (LUAD), Squamous Cell

53   carcinoma (LUSC) and, most rarely, large-cell carcinoma. Lung biopsies are typically used to

54   diagnose lung cancer subtype and stage. Targeted therapies are applied depending on the type

55   of cancer, stage and the presence of sensitizing mutations[1,2]. For example, EGFR (epidermal

56   growth factor receptor) mutations, present in about 20% of LUAD, and ALK mutations (anaplastic

57   lymphoma receptor tyrosine kinase), present in less than 5% of LUAD[3], both have currently

58   targeted therapies approved by the Food and Drug Administration (FDA)[4]. Mutations in other

59   genes, such as KRAS and TP53 are very common (about 25% and 50% respectively), but have

60   proven particularly challenging drug-targets so far[3,5].

61   Virtual microscopy of stained images of tissues are typically acquired at magnifications of x20 to

62   x40, generating very large two-dimensional images (10,000 to over 100,000 pixels in each

63   dimension) that can be tricky to visually analyze in an exhaustive way. Furthermore, accurate

64   interpretation can be difficult and the distinction between LUAD and LUSC is not always clear,

65   particularly in poorly-differentiated tumors, where ancillary studies is recommended for accurate

66   classification. To assist experts, automatic analysis of lung cancer whole-slide images has been

67   recently studied for survival prognosis[6] and classification[7]. In these studies, Yu et al. combined

68   conventional thresholding and image processing techniques with machine learning methods,

69   such as random forest classifiers, SVM or Naïve Bayes classifiers, achieving an Area Under the

70   Curve (AUC) of ~0.85 in distinguishing normal from tumor slides, and ~0.75 in distinguishing

71   LUAD from LUSC slides. Here, we demonstrate how the field can greatly benefit from deep

72   learning, by presenting a strategy based on Convolutional Neural Networks (CNNs) that not only

73   outperforms previously published work, but also achieves accuracies that are at least comparable,

74   if not superior, to human pathologists. The development of new inexpensive and more powerful

75   technologies with higher computing power (in particular Graphics Processing Units, GPUs) has

76   made possible the training of larger and more complex systems[8–10]. This resulted in the design of

77   several deep CNNs, capable of accomplishing complex visual recognition tasks. Such algorithms

78   have already been successfully used for segmentation[11] or classification of medical images[12] and

79   cancers such as breast[13-15], colon cancers[16] or osterosarcoma[17]. CNNs have also been studied

80   for classifying lung patterns on CT (Computerized Tomography) scans, achieving a f-score of

81   ~85.5%[18]. Here, to study the automatic classification of lung cancer tissues, we used the inception

82   v3 architecture[19] and whole-slide images of hematoxylin and eosin stained histopathology images

83   from TCGA obtained by excision. In 2014, Google won the ImageNet Large-Scale Visual

84   Recognition Challenge by developing the GoogleNet architecture[20], derived from the work from

85   Lin et. al[21], which increased the robustness to translation and non-linear learning abilities by using

86   multi-layer perceptrons and global averaging pooling. Inception architecture is particularly useful

87   for processing the data in multiple resolutions, a feature that makes this architecture suitable for

88   pathology tasks. This network has already been successfully adapted to other specific types of

89   classifications like skin cancers[22] and diabetic retinopathy detection[23].

90

91   **Results**

92   We are here comparing several approaches for the classification of tumor slides. First, we

93   employed a strategy similar to the one used by Yu et al.[7], consisting of a two-step binary

94   classification of normal versus tumor slides, followed by a classification of LUAD versus LUSC

95   slides. We then explored a direct classification of the three types of whole-slide images. Finally,

96   we further analyzed LUAD slides to identify which gene mutations could be predicted from those

97   images: we modified and trained the inception v3 architecture on the 10 most common mutations

98   found in the TCGA dataset and related to lung cancer. In this study, we also compare two training

99   approaches: transfer learning versus fully training the inception architecture. In the first case, most

100   of the network keeps the weights learned after the network was trained on object recognition task

101   on the ImageNet dataset, while only the last layer (fully connected layer) of the network is trained.

102   In the second case, the weights are reinitialized randomly, and the network is trained end-to-end,

103   using exclusively lung cancer images.

104

105   ***Fully-trained inception v3 network provides accurate diagnosis (AUC=0.97) of lung***
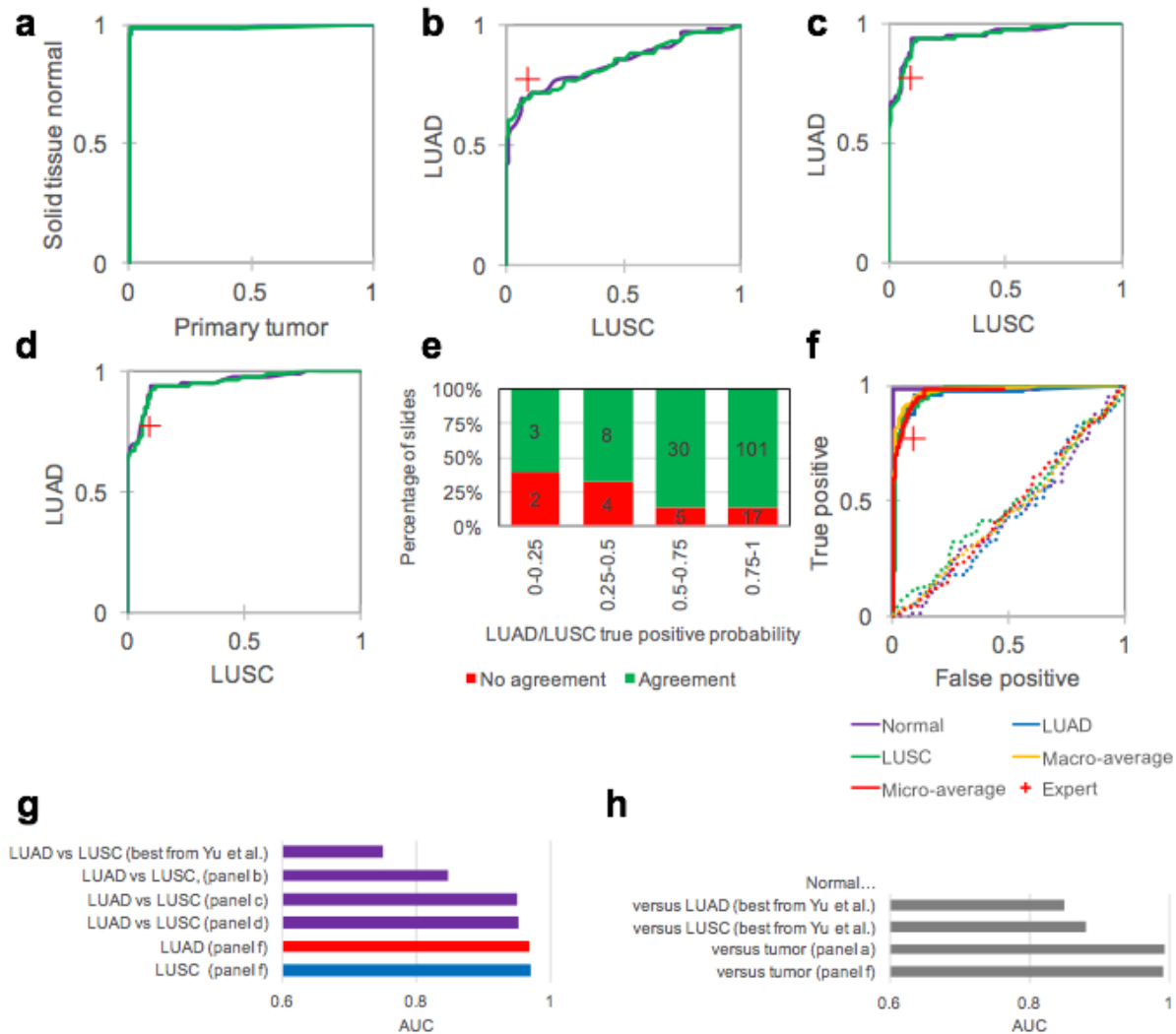
106   ***histopathology images***

107   The TCGA dataset characteristics and our overall computational strategy are summarized in

108   **Figure 1** (see method section for details). We used 1634 whole-slide images from the Genomic

109   Data Commons database: 1176 tumor tissues and 459 normal (**Figure 1a).** These whole-slide

110   images were split into three sets: training, validation and testing (**Figure 1d**). Because the sizes

111   of the whole-slide images are too large to be used as direct input to a neural network (sometimes

112   over 100,000 pixels wide, **Figure 1b**), the network was instead trained, validated and tested using

113   512x512 pixel tiles, obtained from non-overlapping windows of the whole-slide images. This

114   resulted in tens to thousands of tiles per slide depending on the original size (**Figure 1c**). These

115   tiles were first processed individually by the network, and then, per-slide aggregation (see

116   Methods for details) of the results generated a diagnosis for each slide.

117
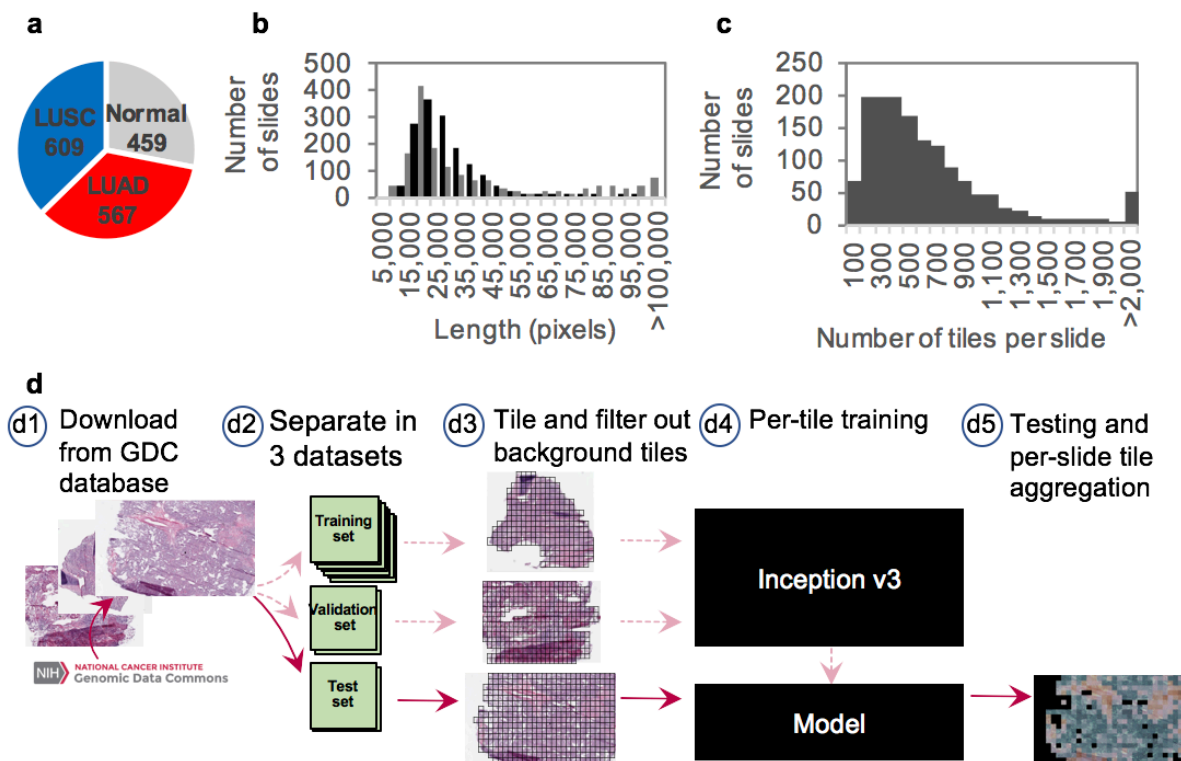
Figure 1. Data and strategy: (a) Number of whole-slide images per class. **(b)** Size distribution of the images widths (gray) and heights (black). **(c)** Distribution of the number of tiles per slide. **(d)** Strategy: **(d1)** Images of lung cancer tissues were first downloaded from the Genomic Data Common database; **(d2)** slides were then separated into a training (70%), a validation (15%) and a test set (15%); **(d3)** slides were tiled by non-overlapping 512x512 pixels windows, omitting those with over 50% background; **(d4)** the Inception v3 architecture was used and partially or fully re-trained using the training and validation tiles; **(d5)** classifications were run on tiles from an independent test set and the results were finally aggregated per slide to extract the heat-maps and the AUC statistics.

Our deep learning approach effectively distinguishes tumor from normal tissue, resulting in a 96.1% per tile accuracy. To assess the accuracy on the test set, the per-tile results were aggregated on a per-slide basis either by averaging the probabilities obtained on each tile, or by counting the percentage of tiles positively classified (**Figure 2a**). This process resulted in an Area Under the Curve (AUC) of 0.990 and 0.993 (**Table 1**) respectively, outperforming the AUC of ~0.85 achieved by the feature-based approach of Yu et al.[7]. Next, we tested the performance of our approach on the more challenging task of distinguishing LUAD and LUSC. First, we tested

135   whether convolutional neural networks can outperform the published feature-based approach,

136   even when plain transfer learning is used. For this purpose, the weights of the last layer of

137   inception v3 – previously trained on the ImageNet dataset to identify 1,000 different classes –

138   were initialized randomly and then trained for our classification task. After aggregating the

139   statistics on a per slide basis (**Figure 2b**), this process resulted in an Area Under the Curve (AUC)

140   of 0.847 (**Table 1**), i.e. a gain of ~0.1 in AUC compared to the best results obtained by Yu et al[7].

141   using image features combined with random forest classifier[7]. The performance can be further

142   improved by fully training inception v3 leading to AUC of 0.947 when aggregation is done by

143   computing the percentage of tiles positively classified, and to AUC of 0.950 when the aggregation

144   is done by averaging the per-tile probabilities (**Figure 2c**). These AUC values are improved by

145   another 0.002 when the tiles previously classified as "normal" by the first classifier are not included

146   in the aggregation process (**Table 1** and **Figure 2d**). The ROC of such a classifier shows

147   performance better than that of a specialist who was asked to classify the images in the test set,

148   independently of the classification provided in TCGA (**Figure 2d**, red cross). About a third of the

149   slides wrongly classified by the algorithm were also misclassified by the specialist, while 85% of

150   those incorrectly classified by the specialist were properly classified by the algorithm (**Figure 2e**).

Figure 2. Accurate classification of lung cancer histopathology images: (a) Per-slide Receiver Operating Characteristic (ROC) curves after classification of normal versus tumor images resulted in an almost error-free classification. Aggregation was either done by averaging the probability scores (purple ROC curves in a to d) or by counting the percentage of properly classified tiles (green ROC curves in a to d). **(b)** The ROC curves obtained after transfer learning for LUAD vs LUSC images classification shows poorer results than when **(c)** the same network has been fully trained. The red crosses correspond to the manual classification by a specialist. **(d)** The ROC curves from (c) is only slightly improved once the tiles classified initially as "normal" have been removed. **(e)** Proportion of slides misclassified by the specialist as a function of the true positive probability assigned in (d). The number of slides are indicated on the bars. **(f)** Multi-class ROC of the Normal vs LUAD vs LUSC classification shows the best result for overall classification of cancer type. Dotted lines are negative control trained and tested after random label assignments. **(g)** Comparison of AUCs obtained with different techniques for classification of cancer type and **(h)** of normal slides.

167 **Figure 3a-r** show heatmap examples for LUAD and LUSC, comparing transfer-learning results

168 with the fully trained network. In the second case, more tiles are true positive and the distribution

169 is more homogeneous, showing for LUSC that almost all of the tiles display LUSC-like features,

170 while for the LUAD, two regions are more prominent with LUAD-like features (one horizontal at

171 the top, one vertical on the left) and some patches showing lower probabilities. Interestingly, most

172 of the LUSC tiles were previously classified as tumor by the first classifier (**Figure 3t**) while for

173 LUAD, the regions with patches having probability near 0.5 in the LUAD/LUSC classification are

174 also those classified as normal with higher probability by the first classifier (**Figure 3s**). We

175 investigated further the use of the deep-learning model by training and testing the network for a

176 direct classification of the three types of images (Normal, LUAD, LUSC in **Figure 2f**). Such an

177 approach resulted in the highest performance with all the AUCs improved to at least 0.968 (**Table**

178 **1**). **Figure 4** shows how the heat-maps are affected by such an approach: the LUSC image shows

179 most of its tiles with a strong true positive probability of LUSC while in the LUAD image, some

180 regions have strong LUAD features, with normal cells on the side (as confirmed by a specialist),

181 and some light blue tiles where LUSC probability is slightly leading.

182

183 **Table 1.** Area Under the Curve (AUC) achieved by the different classifiers

		AUC after aggregation by…	
Classification	**Information**	**… average predicted probability**	**… percentage of positively classified tiles**
Normal vs Tumor	a) Inception v3, fully-trained	0.993	0.990
LUAD vs LUSC	b) Inception v3, transfer learning	0.847	0.847
	c) Inception v3, fully-trained	0.950	0.947

	d) Same as (c) but aggregation done solely on tiles classified as "tumor" by A	0.952	0.949
3 classes. Normal vs LUAD vs LUSC	Normal	**0.991**	NA
	LUAD	**0.968**	NA
	LUSC	**0.971**	NA
	Micro-average	**0.971**	NA
	Macro-average	**0.978**	NA
Mutations	STK11	0.856	0.842
	EGFR	0.826	0.782
	SETBP1	0.775	0.752
	TP53	0.760	0.754
	FAT1	0.750	0.750
	KRAS	0.733	0.716
	KEAP1	0.675	0.659
	LRP1B	0.656	0.657
	FAT4	0.642	0.640
	NF1	0.640	0.632

184

185

186
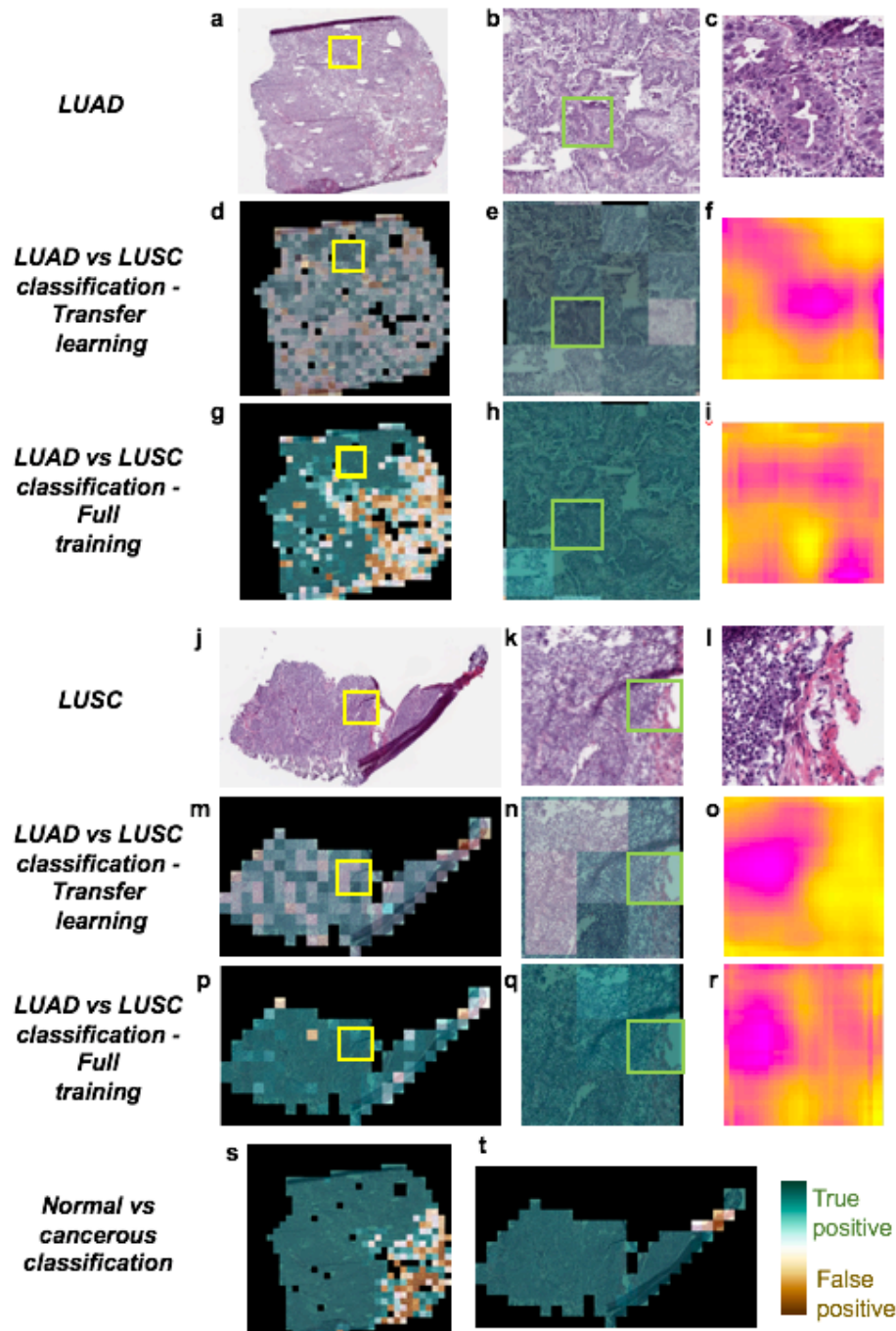
Figure 3. Examples of heatmaps for different binary classifications strategies: (a) Typical slide of Lung Adenocarcinoma (LUAD) tissue. **(b)** Zoom region corresponding to the yellow box in (a). **(c)** Tile corresponding to the green box in (b). **(d)** and **(e)** are the heat-maps corresponding to images (a) and (b), with probability assigned to each tile from brown (false positive) to green (true positive). **(f)** Per-tile heat-map generated after having applied a rolling mask on part of the tile. Yellow pixels show regions not affected by masking while the pink pixels show regions where features were important for proper classification. Images **(d)** to **(f)** were obtained after transfer

195 learning while images **(g)** to **(i)** were obtained after fully training inception v3. Images **(j)** to **(r)**
196 show similar examples for a Lung Squamous Cell (LUSC) tissues. **(s)** and **(t)** show the results of
197 the "normal vs tumor" tiles classifier.
198

199

200
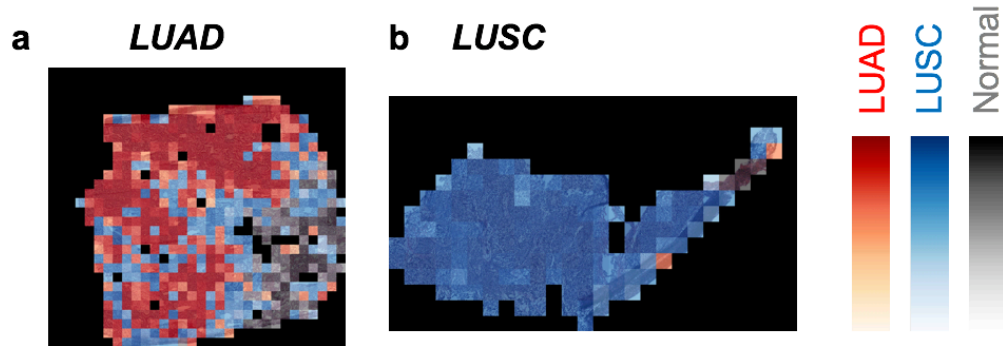
201 **Figure 4. Heatmaps for classification of Normal vs LUAD vs LUSC: (a)** and **(b)** Heatmaps
202 corresponding to images of (**Figure 3a**) and (**Figure 3b**) with probabilities of the winning class
203 assigned to each tile such as: red for tiles classified as LUAD, blue for LUSC and grey for Normal.
204

205

Whole-slide images can predict 6 mutations with an AUC above 0.74

207 The LUAD whole-slide images were further trained to predict gene mutations. Inception v3 was

208 modified to allow multi-output classification and tests were conducted using around 44,000 tiles

209 from 62 slides. Box plot and ROC curves analysis (**Figure 5a-b** and **Figure supp 1**) show that at

210 least six frequently mutated genes seem predictable using our deep learning approach: AUC

211 values for STK11, EGFR, FAT1, SETBP1, KRAS and TP53 were found between 0.733 and 0.856

212 (**Table 1**). As mentioned earlier, EGFR already has targeted therapies. STK11 (Serine/Threonine

213 protein Kinase 11), also known as Liver Kinase 1 (LKB1), is a tumor suppressor inactivated in 15-

214 30% of non-small cell lung cancers[24] and is also a potential therapeutic target: it has been shown

215 on mice that phenformin, a mitochondrial inhibitor, increases survival[25]. Also, it has been shown

216 that STK11 mutations may play a role in KRAS mutations which, combined, result in more

217 aggressive tumors[26]. FAT1 is an ortholog of the Drosophila fat gene involved in many types of

218   cancers and its inactivation is suspected to increase cancer cell growth[27]. Mutation of the tumor

219   suppressor gene TP53 is thought to be more resistant to chemotherapy leading to lower survival

220   rates in small-cell lung cancers[28]. As for SETBP1 (SET 1 binding protein), like KEAP1 and STK11,

221   has been identified as one of the signature mutations of LUAD[29]. Finally, for each gene, we

222   compare the classification achieved by the deep learning approach with the allele frequency

223   (**Figure 5c**). Among the gene mutations predicted with a high AUC, four of them seem to show

224   probabilities related to the allele frequency: FAT1, KRAS, SETBP1 and STK11.

225
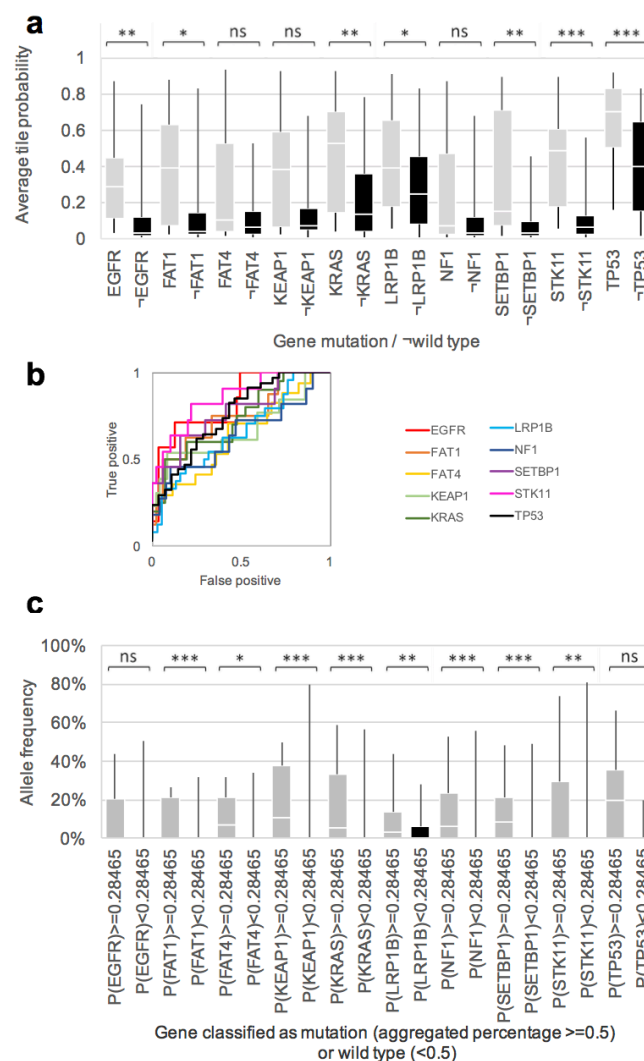
226   **Figure 5. Gene mutation prediction from histopathology slides give promising results for**
227   **at least 6 genes: (a)** Mutation probability distribution for slides where each mutation is present
228   and absent after tile aggregation done by averaging output probability. **(b)** ROC curves associated

229   with (a). **(c)** Allele frequency as a function of slides classified by the deep-learning network as
230   having a certain gene mutation (P≥0.5), or the wild-type (P<0.5). p-values estimated with Mann-
231   Whitney U-test are shown as ns (p>0.05), * (p≤0.05), ** (p≤0.01) or *** (p≤0.001).
232

Discussion

234   The analysis of lung cancer slide images using the inception v3 convolutional neural network

235   shows a clear improvement over classification techniques combining random forest classifiers,

236   SVM or Naïve Bayes classifiers with conventional image processing tools[7] (**Figure 2g-h**). For

237   LUAD vs LUSC classification, while transfer learning outperforms this previous approach by about

238   10% and another ~10% is gained by fully training the network, at the expense of a much longer

239   training period. Finally, another ~2.8% is gained on cancer type classification when "normal"

240   tissues are immediately considered and binary classification is replaced by a direct three-class

241   analysis. This latest approach results in performances slightly better than those achieved by a

242   specialist. It is interesting to notice that around a third of the slides misclassified by the algorithms

243   have also been misclassified by the specialist, showing the intrinsic difficulty to distinguish LUAD

244   from LUSC in some cases. However, 22 out of 26 of the slides misclassified by the specialist were

245   assigned to the correct cancer type by the algorithm showing that it could be beneficial in assisting

246   the specialist in their prognosis. As for classification of normal versus tumor cells, the classification

247   is nearly unambiguous with CNN. Per-slide heat-maps (**Figure 3**) show that true positive tiles

248   appear with a stronger probability when the network has been fully trained. For the LUAD sample,

249   it also shows more consistency with tiles in the same adjacent regions being assigned similar

250   probabilities while the bottom right side of the slide seems to contain less LUAD-like tumor cells

251   according to the classification (**Figure 3g**) and is consistent with visual inspection of that region

252   by a specialist. An example of the important features used for classification of individual is shown

253   for LUAD (**Figure 3f,i**) and LUSC (**Figure 3o,r**). In both cases, the per-tile heat-map of the fully

254   trained network shows a more varied gradient of colors while the tests done after transfer-learning

255   shows more of a binary-like heat-map with regions either very yellow or very pink. The

256   development of appropriate tools for visualizing deep learning models will help in the future to

257   better understand the features used by the classifier[30]. In the current strategy, the only selection

258   used for early tile removal is to make sure that there are enough information and the portion of

259   background present is low. Afterwards, all the remaining tiles belonging to a given slide are used

260   for training and all are associated with the label associated with it. This assumption gives good

261   result since AUCs of 0.95 to 0.97 performance is achieved for LUSC vs LUAD, but it is unlikely

262   that 100% of the tiles are indeed representative of the labelled cancer type. Oftentimes, the tumor

263   is only local and some regions of the slides are not affected by the tumor. Performing an initial

264   classification of "normal" vs "tumor" partially addresses this issue removing normal-like tiles. The

265   fact that these are excisions of lung cancer, the tumor cells spread over the whole slide images

266   available and not a small portion of which has clearly been beneficial for this classification. Finally,

267   it is surprising to note the high AUCs achieved considering that several slides present artifacts

268   inherent to freezing techniques used to prepare those samples. However, it should be noted that

269   the available images may not fully represent the diversity that specialists have to deal with and it

270   may be interesting in the future to assess how the network performs under the less than ideal

271   circumstances that can occur (poor staining quality, focus not optimal or autofocus failure, lack of

272   homogeneity in the illumination, etc). Before this study, it was a priori unclear if and how a given

273   gene mutation would affect the pattern of tumor cells on a whole-slide image but the training of

274   the network using mutated genes as a label lead to very promising prediction results for 6 genes:

275   EGFR, STK11, FAT1, SETBP1, KRAS and TP53. STK11 mutation leads to the highest prediction

276   rate with AUC above 0.85 using aggregation by averaging tile probabilities. Though the number

277   of cases is low (44,000 tiles from 62 test slides), it is interesting to see that our training protocol

278   gives non-random values for several genes, showing that mutation of these particular genes could

279   be predicted from whole-slide images. Hopefully, these predictions will be confirmed once more

280   data are made available. It means that those mutations somehow affect the way the tumor cells

281   look like. Future work on deep-leaning models visualization tools [30] would help identifying those

282 features. These probabilities could be reflecting the percentage of cells effectively affected by the

283 mutation, the allele frequency being significantly higher for at least 4 genes when they were

284 predicted as mutated by the neural network (**Figure 5c**). Looking, for example, at the predictions

285 done on the whole-slide image from **Figure 3a**, our process successfully identifies TP53 (allele

286 frequency of 0.33) and STK11 (allele frequency of 0.33) are two gene most likely mutated (**Figure**

287 **supp 2a**). The heatmap shows that almost all the LUAD tiles are highly predicted as showing

288 TP53-mutatant-like features (**Figure supp 2b**), and two major regions with STK11-mutatant-like

289 features (**Figure supp 2c**). Interestingly, when the classification is applied on all tiles, it shows

290 that even tiles classified as LUSC present TP53 mutations (**Figure supp 2d**) while the STK11

291 mutant is confined to the LUAD tiles (**Figure supp 2e**). These results are realistic since, as

292 mentioned earlier, STK11 is a signature mutations of LUAD [29] while TP53 is more common in

293 human cancers. Being able to predict gene mutations at this stage could be beneficial regarding

294 the importance and impact of those mutations[4,24-29]. This study shows that using deep-learning

295 convolutional neural networks for cancer analysis greatly improve the state-of-the-art automatic

296 classification and could be a very promising tool to assist the specialist in their classification of

297 whole-slide images of lung tissues. Histopathology slides are very large, they usually contain

298 artifacts and be noisy with features of cancer type ambiguous, and making a prognosis manually

299 based on every single region of it can be challenging. Those new techniques can efficiently

300 highlight regions associated with a certain cancer type. Finally, we have shown for the first time

301 the potential to use deep-learning on histopathology images to predict some gene mutations at

302 an early stage.

303

Methods

305 The overall steps described in this section are summarized in **Figure 1** and described in the

306 following sections.

307

Dataset of 1,634 whole-slide images

309 Our dataset comes from the NCI Genomic Data Commons[31] which provides the research

310 community with an online platform for uploading, searching, viewing and downloading cancer-

311 related data. All freely available slide images of Lung cancer were uploaded from this source. We

312 studied the automatic classification of "solid tissue normal" and "primary tumor" slides using a set

313 of respectively 459 and 1175 eosin stained histopathology whole-slide images. Then, the "primary

314 tumor" were classified between LUAD and LUSC types using a set of respectively 567 and 608

315 of those whole-slide images.

316

Image pre-processing generates 987,931 tiles

318 The slides were tiled in non-overlapping 512x512 pixel windows at a magnification of x20 using

319 the openslide library[32] (533 of the 2167 slides initially uploaded were removed because of

320 compatibility and readability issues at this stage). The slides with a low amount of information

321 were removed, that is all the tiles where more than 50% of the surface is covered by background

322 (where all the values are below 220 in the RGB color space). This process generated nearly

323 1,000,000 tiles.

324

325 **Table 2.** Dataset information for normal vs tumor classification: number of tiles / slides in each

326 category.

	Training	Validation	Testing
Normal	132,185 / 332	28,403 / 53	28,741 / 74
Primary tumor	556,449 / 825	121,094 / 181	121,059 / 180

327

328

329 **Table 3.** Dataset information for LUAD vs LUSC classification: number of tiles / slides in each

330 category.

	Training	Validation	Testing
LUAD	255,975 / 403	55,721 / 85	55,210 / 79
LUSC	300,474 / 422	65,373 / 96	65,849 / 91

331

332

Deep learning with Convolutional Neural Network

334 We used 70% of those tiles for training, 15% for validation, and 15% for final testing (**Table 2** and

335 **Table 3**). The tiles associated with a given slide were not separated but associated as a whole to

336 one of these sets to prevent overlaps between the three sets. Typical CNN consist of several

337 levels of convolution filters, pooling layers and fully connected layers. We based our model on

338 inception v3 architecture[19]. This architecture makes use of inception modules which are made of

339 a variety of convolutions having different kernel sizes and a max pooling layer. The initial 5

340 convolution nodes are combined with 2 max pooling operations and followed by 11 stacks of

341 inception modules. The architecture ends with a fully connected and then a softmax output layer.

342 For "normal" vs "tumor" tiles classification, we fully trained the entire network. For the classification

343 of type of cancer, we followed and compared different approaches to achieve the classification:

344 transfer learning, which includes training only the last fully-connected layer, and training the whole

345 network. Tests were implemented using the Tensorflow library (tensorflow.org).

346

Transfer learning on inception v3

348 We initialized our network parameters to the best parameter set that was achieved on ImageNet

349 competition. We then fine-tuned the parameters of the last layer of the network on our data via

350 back propagation. The loss function was defined as the cross entropy between predicted

351 probability and the true class labels, and we used RMSProp[33] optimization, with learning rate of

352 0.1, weight decay of 0.9, momentum of 0.9, and epsilon of 1.0 method for training the weights.

353 This strategy was tested for the binary classification of LUAD vs LUSC.

354

Training the entire inception v3 network

356 The inception v3 architecture was fully trained using our training datasets and following the

357 procedure described in [34]. Similar to transfer learning, we used back-propagation, cross entropy

358 loss, and RMSProp optimization method, and we used the same hyperparameters as the transfer

359 learning case, for the training. In this approach, instead of only optimizing the weights of the fully

360 connected layer, we also optimized the parameters of previous layers, including all the

361 convolution filters of all layers. This strategy was tested on three classifications: normal vs tumor,

362 LUAD vs LUSC and Normal vs LUAD vs LUSC. The training jobs were run for 500,000 iterations.

363 We computed the cross-entropy loss function on train and validation dataset, and used the model

364 with best validation score as our final model. We did not tune the number of layers or hyper-

365 parameters of the inception network such as size of filters.

366

Identification of gene mutations

368 To study the prediction of gene mutations from histopathology images, we modified the inception

369 v3 to perform multi-task classification rather than a single task classification. Each mutation

370 classification was treated as a binary classification, and our formulation allowed multiple

371 mutations to be assigned to a single tile. We optimized the average of the cross entropy of each

372 individual classifier. To implement this method, we replaced the final softmax layer of the network

373 with a sigmoid layer, to allow each sample to be associated with several binary labels [35]. We

374 used RMSProp algorithm for the optimization, and fully trained this network for 500k iterations

375 using only LUAD whole-slide images, each one associated with a 10-cell vector, each cell

376   associated to a mutation and set to 1 or 0 depending on the presence or absence of the mutation.

377   Only the most common mutations were used (**Table 4**), leading to a training set of 223,185 tiles.

378   Training and validation were done over 500,000 iterations (**Figure supp 3**). The test was then

379   achieved on the tiles, and aggregation on the 62 test-slides where at least one of these mutations

380   is present was done only if the tile was previously classified as "LUAD" by the Normal/LUAD/LUSC

381   3-classes classifier.

382

383   **Table 4.** Gene included in the multi-output classification and the percentage of patients with LUAD

384   in the database where the genes are mutated.

Gene mutated	TP53	LRP1B	KRAS	KEAP1	FAT4	STK11	EGFR	FAT1	NF1	SETBP1
%Patients	50	34	28	18	16	15	12	11	11	11

385

386

Results analysis

388   Once the training phase was finished, the performance was evaluated using the testing dataset

389   which is composed of tiles from slides not used during the training. We then aggregated the

390   probabilities for each slide using two methods: either average of the probabilities of the

391   corresponding tiles, or percentage of tiles positively classified. The ROC (Receiver Operating

392   Characteristic) curves and the corresponding AUC (Area Under the Curve) were computed in

393   each case. Tumor slides could contain a certain amount of "normal" tiles. Therefore, we also

394   checked how the ROC & AUC were affected when tiles classified as "normal" were removed from

395   the aggregation. Heat-maps were also generated for some tested slide to visualize the differences

396   between the two approaches and identify the regions associated with a certain cancer type. To

397   visualize the regions of a given tile which were important for the algorithm to take a decision, a

398   rolling mask was applied to the tile. The masked tile was then fed to the network to analyze how

399   the classification is affected. 128x128 pixel overlapping masks were generated over the whole tile

400   with 87.5% overlapping between adjacent masks.

401

Acknowledgments

409

References

411
412   1   *American Cancer Society*, <https://www.cancer.org/> (2017).
413   2   Chan, B. A. & Hughes, B. G. Targeted therapy for non-small cell lung cancer: current
414   standards and the promise of the future. *Translational Lung Cancer Research* **4**, 36-54
415   (2015).
416   3   Terra, S. B. *et al.* Molecular characterization of pulmonary sarcomatoid carcinoma:
417   analysis of 33 cases. *Modern Pathology* **29**, 824-831 (2016).
418   4   Blumenthal, G. M. *et al.* Oncology Drug Approvals: Evaluating Endpoints and Evidence in
419   an Era of Breakthrough Therapie. *The Oncologist* **22**, 762-767 (2017).
420   5   Jänne, P. A. *et al.* Selumetinib plus docetaxel for KRAS-mutant advanced non-small-cell
421   lung cancer: a randomised, multicentre, placebo-controlled, phase 2 study. *The Lancet*
422   *Oncology* **14**, 38-47 (2013).
423   6   Luo, X. *et al.* Comprehensive Computational Pathological Image Analysis Predicts Lung
424   Cancer Prognosis. *Journal of Thoracic Oncology* **12**, 501-509 (2017).
425   7   Yu, K.-H. *et al.* Predicting non-small cell lung cancer prognosis by fully automated
426   microscopic pathology image features. *Nature Communications* **7** (2016).
427   8   Schmidhuber, J. Deep learning in neural networks: An overview. *Neural Networks* **61**,
428   85-117 (2015).
429   9   Hinton, G. E., Osindero, S. & Teh, Y. W. A fast learning algorithm for deep belief nets.
430   *Neural Computation* **18**, 1527-1554 (2006).
431   10   Greenspan, H., Ginneken, B. v. & Summers, R. M. Guest Editorial Deep Learning in
432   Medical Imaging: Overview and Future Promise of an Exciting New Technique. *IEEE*
433   *TRANSACTIONS ON MEDICAL IMAGING* **35**, 1153-1159 (2016).

11   Qaiser, T., Tsang, Y.-W., Epstein, D. & RajpootEma, N. in *Medical Image Understanding and Analysis: 21st Annual Conference on Medical Image Understanding and Analysis.* (ed **Springer International Publishing**).

12   Shen, D., Wu, G. & Suk, H.-I. Deep Learning in Medical Image Analysis. *Annual Review of Biomedical Engineering* **19**, 221-248 (2017).

13   Wang, D., Khosla, A., Gargeya, R., Irshad, H. & Beck, A. H. Deep learning for identifying metastatic breast cancer. *arXiv preprint arXiv:1606.05718* (2016).

14   Cheng, J.-Z. *et al.* Computer-Aided Diagnosis with Deep Learning Architecture: Applications to Breast Lesions in US Images and Pulmonary Nodules in CT Scans. *Scientific Reports* **6** (2016).

15   Cruz-Roa, A. *et al.* Accurate and reproducible invasive breast cancer detection in whole-slide images: A Deep Learning approach for quantifying tumor extent. *Scientific Reports* **7** (2017).

16   Sirinukunwattana, K. *et al.* Locality sensitive deep learning for detection and classification of nuclei in routine colon cancer histology images. *IEEE TRANSACTIONS ON MEDICAL IMAGING* **35**, 1196-1206 (2016).

17   Mishra, R., Daescu, O., Leavey, P., Rakheja, D. & Sengupta, A. in *International Symposium on Bioinformatics Research and Applications.* (ed Springer) 12-23.

18   Anthimopoulos, M., Christodoulidis, S., Ebner, L., Christe, A. & Mougiakakou, S. Lung Pattern Classification for Interstitial Lung Diseases Using a Deep Convolutional Neural Network. *IEEE TRANSACTIONS ON MEDICAL IMAGING* **35**, 1207-1216 (2016).

19   Szegedy, C., Vanhoucke, V., Ioffe, S., Shlens, J. & Wojna, Z. Rethinking the Inception Architecture for Computer Vision. *Proceedings of the IEEE Conference on Computer Vision and Pattern Recognition*, 2818-2826 (2015).

20   Szegedy, C. *et al.* Going Deeper With Convolutions. ***The IEEE Conference on Computer Vision and Pattern Recognition***, 1-9 (2015).

21   Lin, M., Chen, Q. & Yan, S. Network In Network. *ArXiv* **arXiv:1312.4400**, 1-10 (2013).

22   Esteva, A. *et al.* Dermatologist-level classification of skin cancer with deep neural networks. *Nature* **542**, 115-118 (2017).

23   Gulshan, V. *et al.* Development and Validation of a Deep Learning Algorithm for Detection of Diabetic Retinopathy in Retinal Fundus Photographs. *JAMA* **316**, 2402-2410 (2016).

24   Sanchez-Cespedes, M. *et al.* Inactivation of LKB1/STK11 is a common event in adenocarcinomas of the lung. *Cancer Research* **62**, 3659-3662 (2002).

25   Shackelford, D. B. *et al.* LKB1 Inactivation Dictates Therapeutic Response of Non-Small Cell Lung Cancer to the Metabolism Drug Phenformin. *Cancer Cell* **23**, 143-158 (2013).

26   Makowski, L. & Hayes, D. N. Role of LKB1 in lung cancer development. *British Journal of Cancer* **99**, 683-688 (2008).

27   Morris, L. G. *et al.* Recurrent somatic mutation of FAT1 in multiple human cancers leads to aberrant Wnt activation. *Nature genetics* **45**, 253-261 (2013).

28   Mogi, A. & Kuwano, H. TP53 Mutations in Nonsmall Cell Lung Cancer. *Journal of Biomedicine and Biotechnology* **2011**, 9 (2011).

29   Kandoth, C. *et al.* Mutational landscape and significance across 12 major cancer types. *Nature* **502**, 333-339 (2013).

478   30   Zeiler, M. D. & Fergus, R. in *European Conference on Computer Vision.* 818-833.
479   31   Grossman, R. L. *et al.* Toward a Shared Vision for Cancer Genomic Data. *New England*
480   *Journal of Medicine* **375**, 1109-1112 (2016).
481   32   Goode, A., Gilbert, B., Harkes, J., Jukic, D. & Satyanarayanan, M. OpenSlide: A Vendor-
482   Neutral Software Foundation for Digital Pathology. *Journal of Pathology Informatics* **4**,
483   27 (2013).
484   33   Hinton, G., Srivastava, N. & Swersky, K. Lecture 6.5-rmsprop: Divide the gradient by a
485   running average of its recent magnitude. COURSERA: Neural Networks for Machine
486   Learning. (2012).
487   34   *Inception in TensorFlow*, <https://github.com/tensorflow/models/tree/master/inception> (
488   35   Hershey, S. *et al.* in *IEEE International Conference on Acoustics, Speech and Signal*
489   *Processing (ICASSP).*
490